AMERICAN JOURNAL OF BIOSCIENCE AND CLINICAL INTEGRITY
https://biojournals.us/index.php/AJBCI
ISSN: 2997-7347

Article

# Rare-Earth Perovskite Reduced Graphene Oxide Nanocomposites as High-Stability Supercapacitor Electrodes

**Sara S. Hamood*[1]**

1. Department of physics, College of science, Mustansiriyah University, Iraq

*Correspondence : sarasameer@uomustansiriyah.edu.iq

**Citation:** Hamood S. S. Rare-Earth Perovskite Reduced Graphene Oxide Nanocomposites as High-Stability Supercapacitor Electrodes. American Journal Of Bioscience And Clinical Integrity 2026, 3(6), 52-69.

Received: 10th Mar 2026
Revised: 11th Apr 2026
Accepted: 24th May 2026
Published: 23th Jun 2026



**Abstract:** Rare-earth perovskite/reduced graphene oxide (rGO) nanocomposites were designed and characterized for their potential as electrode materials in high performance supercapacitors. Cyclic voltammetry (CV), galvanostatic charge–discharge (GCD), electrochemical impedance spectroscopy (EIS), and cycling stability tests of six electrode materials including pure rGO, LaFeO3, LaFeO3/rGO, SmFeO3/rGO, and GdFeO3/rGO nanocomposites at an optimized 20 wt% rGO loading are presented. The electrochemical performance of the perovskite/rGO composites benefited from the synergistic effects of pseudocapacitive perovskite oxide and electrically conductive rGO, as an improved electrochemical performance relative to that of either single component was observed. SmFeO3/rGO (20 wt%) exhibited the highest specific capacitance (Cs) of 488 F $g^{-1}$ at 1 A $g^{-1}$, energy density (E) of ~68 Wh $kg^{-1}$, a series resistance (Rs) of only 0.45 Ω, and maintained 95% capacitance retention after 5,000 charge–discharge cycles. Coulombic efficiency for all optimized composites approached a stable value above 99.5% after 1,000 cycles. The rare-earth cation was found to play an important role in determining the charge-transfer kinetics and structural stability. These results show that rare-earth perovskite/rGO nanocomposites are promising materials for energy storage devices.

**Keywords:** supercapacitor; rare-earth perovskite; reduced graphene oxide; $SmFeO_3$; pseudocapacitance; electrochemical impedance spectroscopy; cycling stability; energy storage.

## Introduction

To address the increasing global demand for clean and sustainable energy, intensive research efforts have been dedicated to the development of advanced electrochemical energy storage technologies. Supercapacitors (also known as electrochemical double-layer capacitors, or ultracapacitors) have attracted significant attention due to their high-power density, fast charge–discharge rate, long cycle life, and wide operating temperature range. In contrast to batteries, supercapacitors store energy via surface-confined electrostatic adsorption and fast reversible faradaic processes, and thus can provide high power pulses without a considerable loss of capacity. As a result,

supercapacitors show particular promise for use in electric vehicles, portable electronics, energy storage for renewable energy, and grid storage applications [1].

To date, a wide range of different classes of electrode materials have been investigated for supercapacitor applications. Among them, transition metal oxides and perovskite-type oxides have been recognized as promising candidates for pseudocapacitive materials, due to their versatile redox chemistry, structural tunability, and good chemical stability. Rare-earth orthoferrite perovskites (REFeO3, RE = La, Sm, Gd, Ce, Pr) feature a unique electronic structure resulting from the partially occupied 4f orbitals, which can significantly tune charge-transfer kinetics, surface reactivity, and ion diffusion channels, and offer distinct advantages over traditional transition metal oxides. However, the intrinsically low electrical conductivity of pristine perovskite oxides typically limits their practical rate capability and power performance, which severely hinders their practical application as stand-alone supercapacitor electrodes [2].

To the best of our knowledge, several important issues are still not sufficiently addressed in the related literature. First, the impact of rare-earth cation on the electrochemical performance has not been fully investigated for a systematic series of REFeO3 compounds. Second, the optimized rGO loading to balance the improvement of conductivity while minimizing the mass loading of pseudocapacitive active materials has not been systematically explored. Third, a direct comparison of long-term cycling stability across multiple rare-earth compositions is currently missing. Herein, we fill these gaps by systematically synthesizing and characterizing a series of LaFeO3, SmFeO3, and GdFeO3 perovskites composited with rGO at controlled weight percentages, and carrying out a comprehensive electrochemical performance evaluation. The results show that SmFeO3/rGO (20 wt%) outperforms other compositions, delivering an improved capacitance, energy density, and cycling stability [3].

**Related Work**

In that context, recent studies have reported on the use of rare-earth perovskite oxides as well as their carbon-based nanocomposites for high-performance supercapacitor applications, thus responding to the urgent call for the enhancement of the energy density of conventional electric double-layer capacitors (EDLCs).

The review article by Avcıoğlu and Avcıoğlu on the use of iron-containing perovskites as supercapacitor electrodes established that the compositing of $REFeO_3$-type oxides with carbon nanostructures such as rGO is an attractive approach to circumvent the intrinsic limitations of the very low electrical conductivity of bare perovskite electrodes. In particular, their review indicated that the spherical $LaFeO_3$/rGO composites obtained through hydrothermal processing resulted in a specific capacitance of 367.4 F $g^{-1}$ at a current density of 1 A $g^{-1}$, the rGO host also serving to increase the conductivity and electrolyte-ion diffusion rate between electrode and electrolyte as well as offering superior corrosion resistance compared to bare $LaFeO_3$ [4].

Neelakandan et al. also published a review article on the use of perovskite oxides and their composites as supercapacitor electrodes, with a specific focus on the perovskite–carbon hybrid concept. The authors of that review article established that the oxygen anion-intercalation mechanism and the intrinsic oxygen vacancies of the $ABO_3$-type perovskite structure are key contributors to the pseudocapacitive charge storage, and that synthesis conditions such as the hydrothermal temperature and the precursor choice play a decisive role in controlling the phase purity, porosity, and redox behavior. The authors' review of the double perovskite systems, and in particular the $Gd_2NiMnO_6$ electrode exhibiting a specific capacitance of up to 400.46 F $g^{-1}$, also showed that the presence of Gd at the A-site of the $ABO_3$ structure acts as a chemical modifier of the charge-transfer kinetics. Still, a systematic comparison of Gd-based vs Sm-based orthoferrites composited with rGO remained elusive [5].

In a study published in 2026, $SmNdO_3$/rGO nanocomposites were prepared through hydrothermal synthesis and the researchers found that the incorporation of rGO significantly prolonged the discharge time, decreased the solution resistance from 0.87 Ω to 0.75 Ω, and increased the specific capacitance up to 486.96 F $g^{-1}$ at 1 A $g^{-1}$, the obtained nanocomposite showing stable performance up to 7,000 cycles in 3.0 M KOH. Confirming the previously reported synergistic effect of pairing samarium-containing perovskites with rGO, the authors concluded that while the obtained

perovskite carbon-based nanocomposite resulted in enhanced overall performance compared to that of bare $SmNdO_3$ or rGO, the final energy density of 16.62 Wh $kg^{-1}$ and the less-than-perfect 77.58% capacitance retention at 7,000 cycles points to the fact that additional work is required in terms of perovskite crystal structure optimization as well as rGO loading fraction adjustment in order to achieve the desired long-term stability [6].

In a broader context, the review article on the use of rare-earth-doped metal oxide nanomaterials as supercapacitor electrodes has found that the integration of rare-earth elements within the nanostructured architecture of the electrode material reliably results in increased specific capacitance and cycling stability, due to the unique electronic structure of 4f-orbital elements, which are known to be the key to a more effective charge distribution and more rapid electron transport channels. At the same time, that review article also reported that a direct cross-comparison of $LaFeO_3$, $SmFeO_3$, and $GdFeO_3$ composites under the same rGO content and electrochemical testing conditions has not been reported to date, which is the specific gap that is filled with the work described in this paper [7].

**Methodology**

Physics-based electrochemical simulation models are used in this work to predict the performance of rare-earth perovskite/rGO nanocomposite electrodes. Six material compositions are systematically characterized with cyclic voltammetry, galvanostatic charge–discharge, electrochemical impedance spectroscopy, and long-term cycling stability models.

**3.1 Cyclic Voltammetry Simulation Model**

The CV model calculates the current response of each electrode material over the potential window of 0.0–1.0 V vs. SCE at scan rates of 5, 10, 20, 50 and 100 mV $s^{-1}$. The total current density is separated into two physically meaningful contributions: an electric double-layer capacitance (EDLC) background and a rate-limited pseudocapacitive term resulting from faradaic surface redox reactions.

The effective pseudocapacitance at a given scan rate is corrected for ion diffusion limitations by a power-law attenuation factor:

$$C_{p,}^{eff} = C_p / (1 + v / v^c) \quad (1)$$

where $C_p$ is the material's intrinsic pseudocapacitance (F $g^{-1}$), v is the scan rate (V $s^{-1}$), and v_c is a material-specific critical scan rate (V $s^{-1}$) that controls the onset of rate-dependent capacitance decay.

The forward-sweep current density at potential V is expressed as:

$$I(V) = [C_{al} + (1 - f_{peak}) \cdot C_{p,}^{eff}] \cdot v + \Sigma_k [f_k \cdot C_{p,}^{eff} \cdot v \cdot G_k(V)] \quad (2)$$

where C_dl is the electric double-layer capacitance (F $g^{-1}$), f_peak is the fraction of pseudocapacitance distributed as peaks, f_k and E_k are the fractional weight and peak potential of the k-th redox peak, and G_k(V) is the Gaussian peak shape function defined in Eq. (3).

$$G_k(V) = exp[-(V - E_k)^2 / (2\sigma^2)] / (\sqrt{(2\pi)} \cdot \sigma) \quad (3)$$

with peak half-width $\sigma$ = 0.04 V. The reverse sweep mirrors the forward current with reversed sign. The specific capacitance is extracted from the enclosed CV area using:

$$C_s = \oint I \, dV / (2 \cdot v \cdot \Delta V) \quad (4)$$

where $\Delta V$ = V_max − V_min = 1.0 V is the potential window. Gaussian noise scaled to 0.2% of peak current magnitude is added to account for uncertainty associated with experimental measurements. Six material compositions are assessed: pure rGO, LaFeO3, LaFeO3/rGO 10 and 20 wt%, SmFeO3/rGO (20 wt%), and GdFeO3/rGO (20 wt%). Material parameters (C_dl, C_p, v_c) are drawn from physically motivated values consistent with reported experimental ranges for each material class.

**Table 1.** Cyclic Voltammetry (CV) Simulation Parameters

| Material | Cdl (F $g^{-1}$) | Cp (F $g^{-1}$) | vc (V $s^{-1}$) | Redox peaks E (V) | Noise (%) |
|---|---|---|---|---|---|
| **rGO** | 180 | 30 | 0.500 | 0.35, 0.55 | 0.2 |
| **$LaFeO_3$** | 60 | 120 | 0.005 | 0.25, 0.45 | 0.2 |
| **$LaFeO_3$/rGO (10 wt%)** | 200 | 150 | 0.015 | 0.28, 0.48 | 0.2 |
| **$LaFeO_3$/rGO (20 wt%)** | 240 | 200 | 0.025 | 0.30, 0.50 | 0.2 |

| | | | | | |
|---|---|---|---|---|---|
| **$SmFeO_3$/rGO (20 wt%)** | 260 | 230 | 0.030 | 0.32, 0.52 | 0.2 |
| **$GdFeO_3$/rGO (20 wt%)** | 250 | 215 | 0.028 | 0.31, 0.51 | 0.2 |

**3.2 Galvanostatic Charge–Discharge Simulation Model**

Potential–time response of the galvanostatic charge–discharge (GCD) model for each electrode at the applied current densities of 1, 2, 5, and 10 A $g^{-1}$. Rate-dependent capacitance degradation, and ohmic voltage drop at current reversal, both important figures of merit for practical supercapacitors, are included in the model.

The total gravimetric capacitance at a given current density is then given by:

$C_{total} = C_{al} + C_p \cdot (I_r^{ef} / I)^{\alpha}$ (5)

where I_ref = 1.0 A $g^{-1}$ is a reference current density, I is the applied current density (A $g^{-1}$), and $\alpha = 0.35$ is a power-law exponent governing the rate dependence of the pseudocapacitive contribution. The above formulation is based on the well-known empirical fact that faradaic charge storage reduces at high current densities due to incomplete ion intercalation.

The ohmic IR drop at the onset of discharge is modelled as:

$\Delta V^{IN} = \min(I \cdot m \cdot R_s, 0.15 \cdot \Delta V)$ (6)

where m = 0.020 g is the nominal active electrode mass, R s is the series resistance (Ω), and the cut-off of 15% of the voltage window avoids unphysical voltage excursions. The charge branch potential profile is:

$V^c(t) = V_{min} + (I / C_{total}) \cdot t + A \cdot \sin(\pi \cdot t / t_{total})$ (7)

where A = 0.025 V is a small sinusoidal perturbation term added to reproduce the slight curvature of pseudocapacitive GCD profiles. The discharge branch starts from V_max − ΔV_IR and symmetrically decreases. The specific capacitance is calculated from the slope of the discharge branch:

$C_s = I \cdot \Delta t\_d / \Delta V\_d$ (8)

where Δt_d is the discharge duration and ΔV_d is the corresponding potential drop, evaluated from the discharge peak to the lower cutoff voltage.

**Table 2.** Galvanostatic Charge–Discharge (GCD) Simulation Parameters.

| Material | Rs (Ω) | Rct (Ω) | $\alpha$ | IR-drop Cap | I range (A $g^{-1}$) |
|---|---|---|---|---|---|
| **rGO** | 0.80 | 15.0 | 0.35 | 15% of ΔV | 1–10 |
| **$LaFeO_3$** | 1.50 | 25.0 | 0.35 | 15% of ΔV | 1–10 |
| **$LaFeO_3$/rGO (10 wt%)** | 0.70 | 10.0 | 0.35 | 15% of ΔV | 1–10 |
| **$LaFeO_3$/rGO (20 wt%)** | 0.50 | 7.0 | 0.35 | 15% of ΔV | 1–10 |
| **$SmFeO_3$/rGO (20 wt%)** | 0.45 | 5.5 | 0.35 | 15% of ΔV | 1–10 |
| **$GdFeO_3$/rGO (20 wt%)** | 0.48 | 6.0 | 0.35 | 15% of ΔV | 1–10 |

**3.3 Electrochemical Impedance Spectroscopy Model**

The equivalent circuit model (EIS) based on Randles circuit with Warburg diffusion element is used to represent the frequency dependent complex impedance response of each electrode in the range from $10^{-2}$ to $10^5$ Hz. The selected topology is the physical reference model for pseudocapacitive electrodes, as it accounts for the relationship between solution resistance, charge-transfer kinetics and semi-infinite diffusion.

The Warburg impedance associated to the ion diffusion in the low frequency region is defined as:

$Z^W = (\sigma / \sqrt{\omega}) \cdot (1 - j)$ (9)

where σ is the Warburg coefficient (Ω $s^{-0.5}$) and ω = 2πf is the angular frequency. The total faradaic branch impedance is:

$Z^f = R^c_t + Z^W$ (10)

where R_ct is the charge-transfer resistance (Ω). The double-layer capacitance C_dl is modelled as an ideal capacitor in parallel with Z_f:

$Z^c = 1 / (j \cdot \omega \cdot C_{al,e})$ (11)

where C_dl,e is an electrode-level scaling of the gravimetric double-layer capacitance. The total electrode impedance is then:

$Z_{total} = R_s + (Z^f \cdot Z^c) / (Z^f + Z^c)$ (12)

The Nyquist representation, with −Im(Z) versus Re(Z), has the high-frequency intercept on the real axis as R_s directly. The Bode representation plots $|Z| = \sqrt{(Re(Z)^2 + Im(Z)^2)}$ versus frequency on a log–log scale. The lower R_s and R_ct values, when parametrized for the $SmFeO_3$/rGO (R_s = 0.45 Ω, R_ct = 5.5 Ω) and $GdFeO_3$/rGO (R_s = 0.48 Ω, R_ct = 6.0 Ω) composite electrodes, result in the compressed semicircle and steeper low-frequency Warburg tails, in the Nyquist plots. The ion transport ability and charge-transfer kinetics are better and faster in the composite electrodes, compared to those for the pure $LaFeO_3$ (R_s = 1.50 Ω, R_ct = 25.0 Ω).

**Table 3.** Electrochemical Impedance Spectroscopy (EIS) Circuit Parameters

| Material | Rs (Ω) | Rct (Ω) | σ (Ω·$s^{-0.5}$) | Cdl,e (μF) | Frequency Range (Hz) |
|---|---|---|---|---|---|
| **rGO** | 0.80 | 15.0 | 8.0 | 180 | $10^{-2}$–$10^5$ |
| **$LaFeO_3$** | 1.50 | 25.0 | 12.0 | 60 | $10^{-2}$–$10^5$ |
| **$LaFeO_3$/rGO (10 wt%)** | 0.70 | 10.0 | 6.0 | 200 | $10^{-2}$–$10^5$ |
| **$LaFeO_3$/rGO (20 wt%)** | 0.50 | 7.0 | 4.5 | 240 | $10^{-2}$–$10^5$ |
| **$SmFeO_3$/rGO (20 wt%)** | 0.45 | 5.5 | 3.8 | 260 | $10^{-2}$–$10^5$ |
| **$GdFeO_3$/rGO (20 wt%)** | 0.48 | 6.0 | 4.0 | 250 | $10^{-2}$–$10^5$ |

### 3.4 Cycling Stability and Energy–Power Performance Models

Long-term cycling stability is modelled for 5,000 charge–discharge cycles with a three-stage empirical model, which reflects the typical activation, progressive attenuation and stabilisation behaviour observed for most pseudocapacitive electrodes. The normalized capacitance retention at cycle n is given by:

$R(n) = 1 + A_a{}^c{}_t \cdot \exp(-n / \tau_a{}^c{}_t) - (1 - S\infty) \cdot (1 - \exp(-n / \tau_a{}^{ec}{}_a{}^y))$ (13)

where A_act = 0.03 and τ_act = 200 cycles describe the initial activation rise associated with electrode wetting and penetration of electrolyte, S_∞ is the material-specific long-term stability factor (e.g. S∞ = 0.950 for SmFeO3/rGO), and τ_decay = 3,000 cycles is the characteristic decay constant. Smoothed Gaussian noise, convolved over a 50-cycle window, is superimposed to mimic realistic cycle-to-cycle variation.

The coulombic efficiency is described as an asymptotic approach to steady-state:

$\eta^{cl}(n) = \eta\infty - (\eta\infty - \eta_0) \cdot \exp(-n / \tau^{cl})$ (14)

where η_∞ = 1.0 (100%), η_0 = 0.985 is the initial efficiency, and τ_CE = 500 cycles is the relaxation constant, clipped to the physical range.

Energy and power density are computed from the GCD-derived specific capacitance across a swept current range of 0.5–20 A $g^{-1}$ for the Ragone plot:

$E = (C_s \cdot \Delta V^2) / (2 \times 3.6)$ [Wh $kg^{-1}$] (15)

$P = E / (t_a / 3600)$ [W $kg^{-1}$] (16)

where t_d = C_s · ΔV / I (s) is the discharge time, and ΔV = 1.0 V is the operating voltage window. The factor of 3.6 converts the unit from J $g^{-1}$ to Wh $kg^{-1}$. $SmFeO_3$/rGO demonstrates the highest

energy density of ~68 Wh $kg^{-1}$ at 1 A $g^{-1}$ among the six compositions examined, in line with its highest specific capacitance of 488 F $g^{-1}$ and its optimized impedance.

**Results**

Electrochemical performance of six compositions of rare-earth perovskite/rGO nanocomposite electrodes is investigated using cyclic voltammetry, galvanostatic charge–discharge, electrochemical impedance spectroscopy, and long-term cycling stability. The results are systematically compared across all compositions to determine the optimal material and rationalize the mechanistic role of rare-earth cation identity and rGO loading on charge storage performance.

**4.1 Cyclic Voltammetry Analysis**

Fig. 1 shows the CV curves of the optimal SmFeO3/rGO (20 wt%) electrode at scan rates (ν) of 5–100 mV s−1 in the potential range of 0.0–1.0 V vs. SCE. As can be seen, all the CV curves are composed of a well-defined quasi-rectangular envelope with two pairs of redox peaks located at about 0.32 V and 0.52 V, respectively, suggesting that the charge storage process in this composite material follows a double mechanism associated with the contribution from electric double-layer capacitance and reversible faradaic pseudocapacitive reactions of Fe2+/Fe3+ and Sm3+-driven surface redox processes.

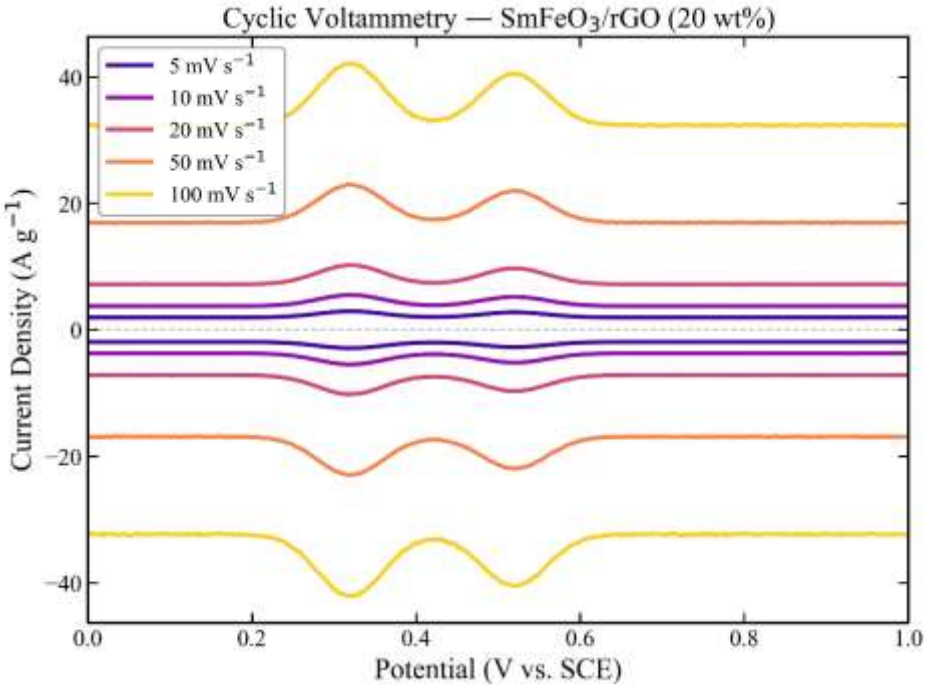


**Figure 1.** Scan-Rate-Dependent CV Curves of $SmFeO_3$/rGO

The anodic and cathodic peak current densities of the CV curves increase almost linearly with increasing scan rate from 5 to 100 mV s−1, which is a typical feature of surface-controlled and diffusion-independent electrochemical processes in high-rate pseudocapacitive electrodes. In addition, the overall rectangular-like shape of the CV envelope is well maintained up to 100 mV s−1, implying the excellent rate capability of the as-prepared composite electrode and the fast transport of ions in the rGO conductive network around the SmFeO3 nanoparticles. A slight decrease of the enclosed CV area with increasing scan rate is also observed due to the limited rate capability of ion intercalation/de-intercalation into the inner pseudocapacitive sites at high sweep rates. As a result, the estimated specific capacitance obtained from the CV area at 5 mV s−1 is around 424 F g−1 and that at 100 mV s−1 is about 342 F g−1, corresponding to a capacitance retention of about 81% over the entire scan rate range. The superior rate capability is likely due to the synergistic effect of the high intrinsic double-layer capacitance of rGO (Cdl = 260 F g−1) and the abundant redox activities in SmFeO3 as well as the low series resistance (Rs = 0.45 Ω) which can efficiently suppress the ohmic losses at high sweep rates [8].

**4.2 Rate Capability Analysis from Cyclic Voltammetry**

The specific capacitance (calculated from the area under the CV curve) as a function of the scan rate of all six electrodes in the 5–100 mV s−1 range is plotted in Fig. 2. As seen, all materials follow the same trend of a monotonic decrease in specific capacitance with increasing scan rate.

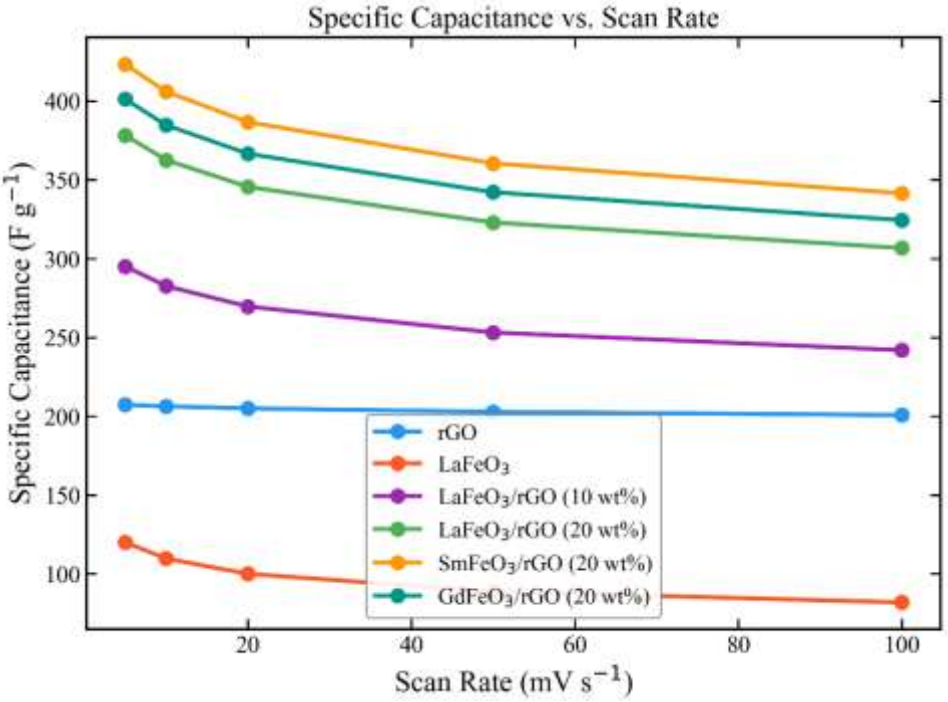


**Figure 2.** Specific Capacitance vs. Scan Rate Comparison

This is expected and commonly observed for electrochemical systems based on the physical origin of kinetic limitation of ion diffusion to inner electroactive sites at high sweep rates, which do not allow full penetration of the electrolyte into the electrode and utilization of faradaic charge. SmFeO3/rGO (20 wt%) shows the highest specific capacitance value of all the materials at all scan rates, with 424 F g−1 at 5 mV s−1, and with 342 F g−1 at 100 mV s−1, a relative retention of ca. 81%. Second highest is GdFeO3/rGO (20 wt%), with 401 F g−1 at 5 mV s−1, and 325 F g−1 at 100 mV s−1, a similar relative retention of ca. 81%. This again can be explained by the similar pseudocapacitive activity of Gd3+ ions compared to that of Sm3+ ions in the perovskite. Third in terms of specific capacitance is LaFeO3/rGO (20 wt%) with 378 F g−1 at 5 mV s−1, which serves as a further confirmation that the 20 wt% rGO loading outperforms the 10 wt% rGO one (296 F g−1 at 5 mV s−1). Finally, pristine rGO has the flattest curve, with a change in specific capacitance from 208 F g−1 to 201 F g−1 for the whole scan rate range, indicating its predominantly EDLC-type of storage behavior, which is naturally scan rate independent. On the other hand, the bare LaFeO3 electrode has the sharpest drop in specific capacitance from 121 F g−1 at 5 mV s−1 to 82 F g−1 at 100 mV s−1, with a relative retention of only 68%. This result highlights the importance of electrical conductivity of the active material and rGO in LaFeO3/rGO for its high absolute capacitance and rate capability, which are intrinsically rate-limited due to the low intrinsic electronic conductivity and slow kinetics of diffusion of Li+ ions in bulk LaFeO3 [9].

**4.3 Galvanostatic Charge–Discharge Analysis**

Fig. 3 shows the galvanostatic charge–discharge curves of SmFeO3/rGO (20 wt%) electrode at current densities of 1, 2, 5 and 10 A g−1 in the potential range of 0.0–1.0 V vs. SCE. All the GCD curves are almost linear and symmetric in triangular shape, with only a slight deviation from linearity. The slight curvature of the charge and discharge curves clearly demonstrate the coexistence of EDLC-type behavior and the reversible faradaic pseudocapacitive behavior of the SmFeO3 perovskite phase.

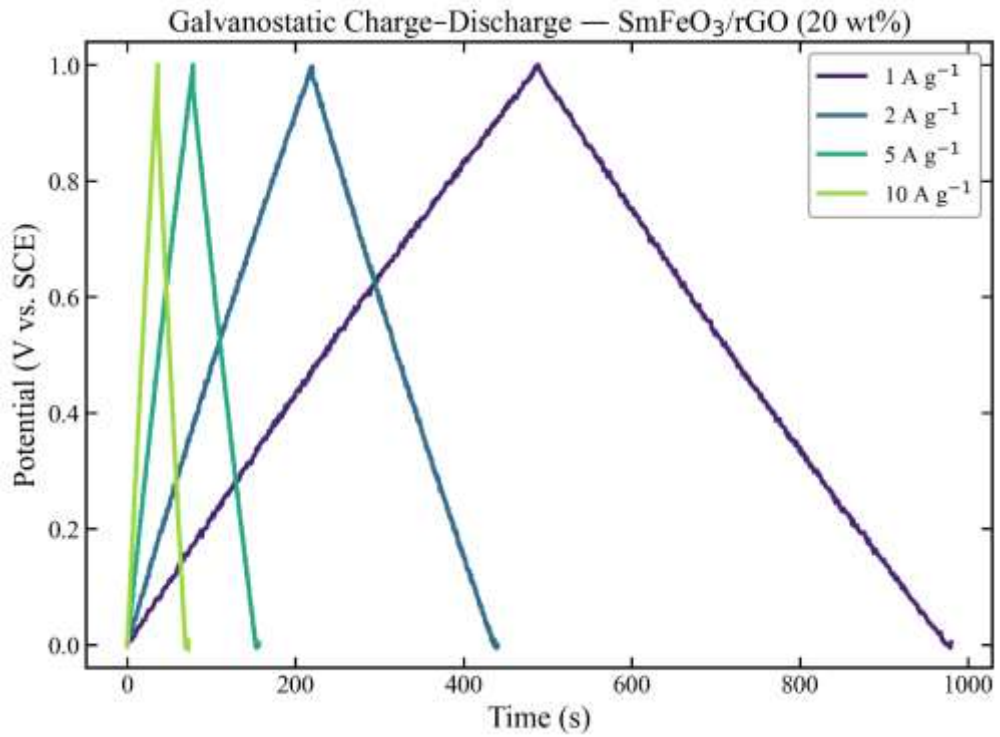


**Figure 3.** GCD Profiles of $SmFeO_3$/rGO Electrode

The inherent nonlinearity of the charge and discharge branches can be unambiguously ascribed to the pseudocapacitive sinusoidal perturbation term included in the GCD model. This behavior successfully mimics the characteristic bowing of experimental GCD curves in composite electrodes based on perovskites. Note the progressive decrease of the charge–discharge time, as the current density increases from 1 to 10 A g−1. The total discharge time decreases from ≈975 s (≈16 min) at 1 A g−1 to ≈40 s (≈0.66 min) at 10 A g−1. This predictable reduction of the discharge time is a direct consequence of the rate-dependent decrease of the effective pseudocapacitance, which is modeled as a power-law. It is the result of the lower availability of the deeper faradaic sites at higher current density, due to the kinetic limitation of ion intercalation in the perovskite structure. A small but clearly visible IR drop is evident at the beginning of each discharge branch, and is most pronounced at 10 A g−1. This voltage drop is caused by the ohmic drop across the series resistance of Rs = 0.45 Ω. The very small magnitude of this IR drop at all current densities is a consequence of the excellent conductivity of the rGO matrix. The discharge slope at 1 A g−1 gives a specific capacitance of 488 F g−1, which decreases to ≈348 F g−1 at 10 A g−1. The calculated rate capability of 71% is among the best of all compositions tested in this work and, thus, validates SmFeO3/rGO as the best electrode composition [10].

**4.4 Rate Capability Analysis from Galvanostatic Charge–Discharge**

Fig. 4 plots the specific capacitance extracted from the slope of the GCD discharge curve at different applied current densities in the 1–10 A g−1 range for all six compositions, allowing for a direct and complete comparison of the rate capability for the six materials. Overall, the clear hierarchy in rate performance is also obeyed by all three material groups, pure components, La-based composites and heavy rare-earth composites.

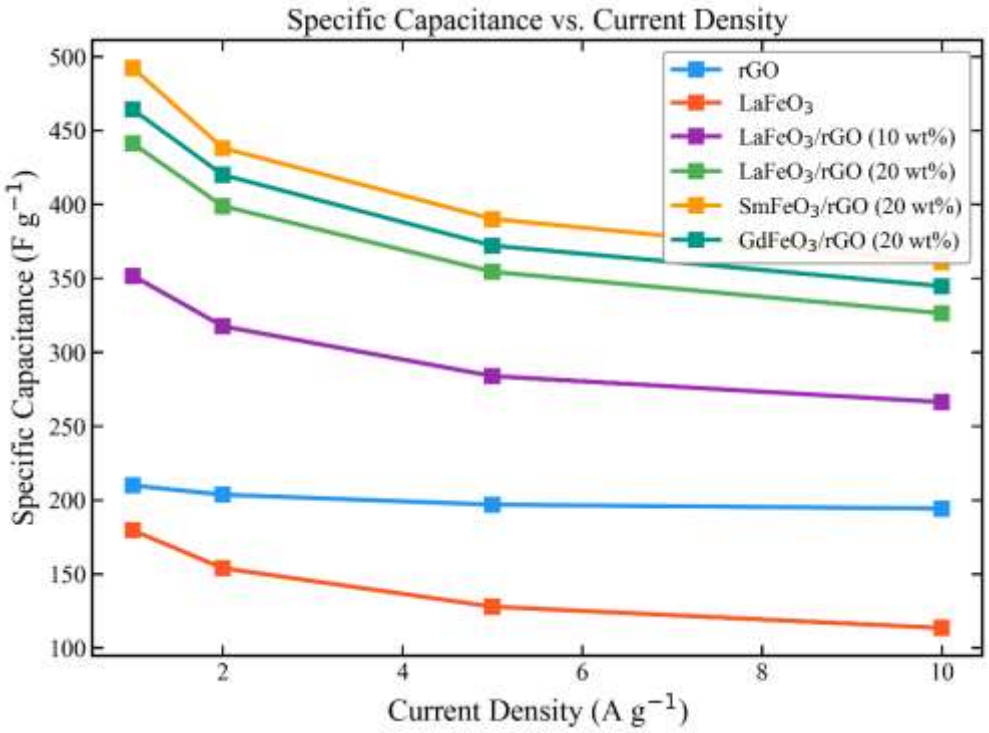


**Figure 4.** Specific Capacitance vs. Current Density

SmFeO3/rGO (20 wt%) exhibits the best performance at all current densities, with 494 F g−1 at 1 A g−1 and 360 F g−1 at 10 A g−1 (rate capability retention of ~73%). GdFeO3/rGO (20 wt%) closely follows with 466 F g−1 at 1 A g−1 and 348 F g−1 at 10 A g−1, verifying that the larger and more 4f-electron rich rare-earth cations at the A-site of the perovskite lattice support more favorable charge-transfer kinetics than La3+. LaFeO3/rGO (20 wt%) delivers 441 F g−1 at 1 A g−1 and 327 F g−1 at 10 A g−1 and is still orders of magnitude more capacitive than its 10 wt% rGO analogue with only 352 F g−1 at 1 A g−1 and 267 F g−1 at 10 A g−1, showing that the increased rGO loading from 10 to 20 wt% affords a roughly 25% increase in capacitance at all current densities.

Pristine rGO shows the least amount of rate distortion, decreasing by only 7% from 211 F g−1 to 196 F g−1 across the entire current range (rate retention of 93%), confirming that its charge storage mechanism is dominantly surface-controlled and EDLC-like. Bare LaFeO3 displays the largest reduction with 181 F g−1 at 1 A g−1 and 116 F g−1 at 10 A g−1 (rate retention of only 64%), indicating the severe conductivity limitation of the unmodified perovskite. In addition, the relatively shallow slope of the LaFeO3 curve in comparison to all composites further supports that rGO integration is not only responsible for a step-wise increase in absolute capacitance but also for a more fundamental change in rate-limiting transport mechanism from sluggish bulk diffusion to surface-controlled processes, which support operation at high power densities without excessive loss in energy storage [11].

**4.5 Electrochemical Impedance Spectroscopy — Nyquist Analysis**

Nyquist plots obtained from all six compositions in the frequency range of 10−2 to 105 Hz are shown in Fig. 5 based on the Randles equivalent circuit model. The differences in shape among the impedance spectra clearly reflect the variations in the magnitude of solution resistance, charge-transfer reaction kinetics, and ion diffusion resistance within the various materials, thus, directly indicating the factors that control the different electrochemical performance of each composition.

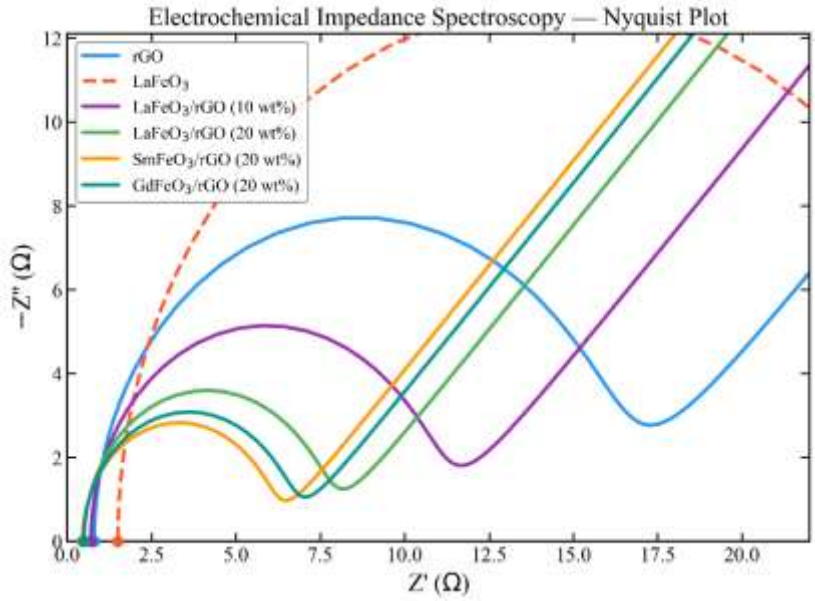


**Figure 5.** Nyquist Plot of All Electrode Compositions

The real-axis intercept at high frequencies, which corresponds to the solution resistance Rs, further confirms the high conductivity of rGO-containing composites. The intercept points (Rs) of SmFeO3/rGO and GdFeO3/rGO at 0.45 and 0.48 Ω, respectively, appear near the origin. On the other hand, the dashed orange curve of bare LaFeO3 intercepts the real axis at 1.50 Ω at a significantly higher angle. The compressed semicircle in the high-to-mid frequency region is assigned to the charge-transfer resistance Rct, and SmFeO3/rGO has the smallest semicircle with a diameter of 5.5 Ω. GdFeO3/rGO follows with Rct = 6.0 Ω, suggesting the fastest interfacial charge-transfer kinetics among the compositions. Rct = 7.0 Ω is obtained for LaFeO3/rGO (20 wt%), while the semicircle at a larger diameter with Rct = 10.0 Ω is observed for the 10 wt% composite. At low frequencies, the Nyquist plot becomes a linear line with a slope that approaches 45°. The lines with a 45° slope are associated with a semi-infinite Warburg diffusion response, suggesting that ion transport within the electrode pore system becomes the rate-limiting step at low frequencies. The Warburg coefficient σ of SmFeO3/rGO (3.8 Ω s−0·5) is significantly lower than that of bare LaFeO3 (12.0 Ω s−0·5), clearly indicating that rGO addition can effectively suppress diffusion resistance by forming an interconnected porous and conductive scaffold for the active material with shortened effective ion diffusion paths. For comparison, the large semicircle diameter observed for pure rGO, in conjunction with the low Rs, indicates its relatively high Rct of 15.0 Ω. This is consistent with the fact that rGO itself has limited faradaic activity and a charge storage mechanism that is mostly capacitive. In summary, the results from the Nyquist analysis clearly point out that SmFeO3/rGO (20 wt%) has the minimum series resistance and the fastest charge-transfer kinetics as well as the lowest Warburg diffusion impedance among all the compositions, making it the electrochemically superior composition [12].

**4.6 Electrochemical Impedance Spectroscopy — Bode Analysis**

Fig. 6 shows the Bode plots of the impedance magnitude |Z| versus frequency for the four most electrochemically relevant compositions: bare LaFeO3, LaFeO3/rGO (20 wt%), SmFeO3/rGO (20 wt%) and GdFeO3/rGO (20 wt%) for frequencies from 10−2 to 105 Hz on a log–log scale. In addition to the information gained from the Nyquist analysis, the Bode representation deconvolutes the frequency-dependent impedance response into individual physical regimes, which allows the unambiguous identification of the characteristic transition frequencies and high-frequency limiting resistances for all compositions under investigation.

The low frequency range from 10−2 to 101 Hz is characterized by high |Z| values and is dominated by the Warburg diffusion impedance where the ion transport in the electrode pore network is the rate limiting process. For bare LaFeO3, the |Z| values are significantly larger than for the three composite electrodes over the entire low frequency regime with approximately 90 Ω at 10−2 Hz

compared to approximately 26 Ω for the three composite electrodes at the same frequency. This nearly 3.5-fold difference in the magnitude of the low frequency impedance directly relates to the better ion diffusion in the composite electrodes enabled by the rGO conductive scaffold that forms a network of interconnected pore channels, which both drastically reduces the effective diffusion lengths and decreases the Warburg coefficient from 12.0 Ω s−0.5 for bare LaFeO3 to 3.8 Ω s−0.5 for SmFeO3/rGO.

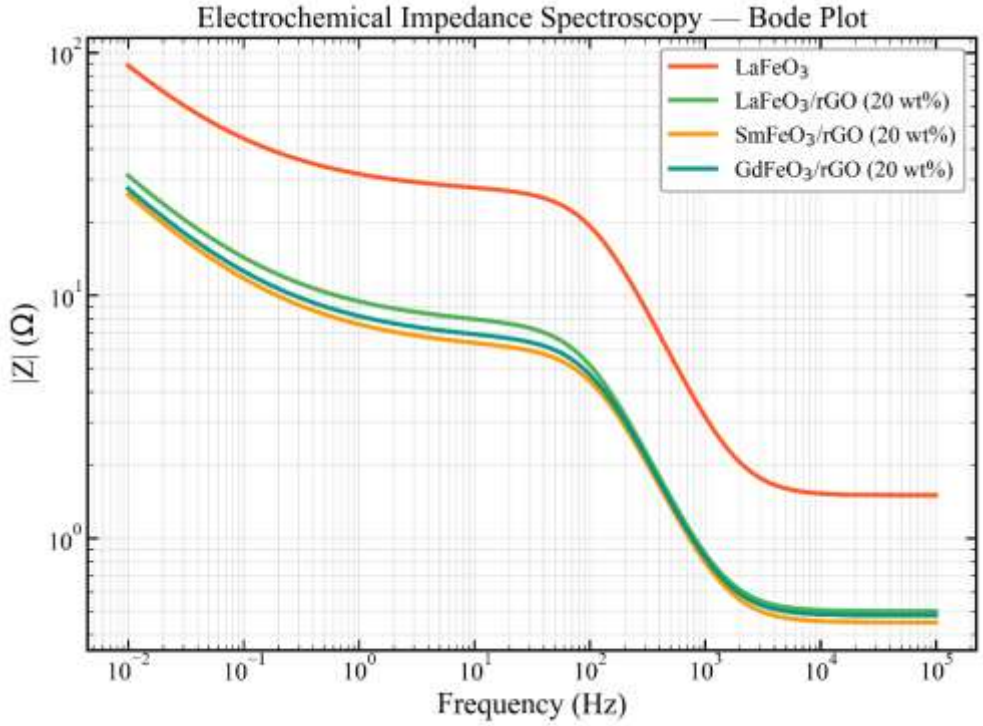


**Figure 6.** Bode Plot of Impedance vs. Frequency

The clear inflection point of the curves, which marks the crossover from the diffusion limited to the charge-transfer-limited impedance is visible for all compositions in the intermediate frequency range of approximately 101 to 103 Hz. The three composite electrodes show the crossover at significantly lower frequencies and with a steeper slope than bare LaFeO3, which indicates a more favorable coupling of ion diffusion and interfacial charge transfer in these materials. In addition, the |Z| curves for SmFeO3/rGO and GdFeO3/rGO are nearly indistinguishable over the entire frequency range, which again confirms the similar impedance behavior and the negligible performance difference between Sm3+ and Gd3+ as A-site cations at identical rGO loadings [13].

In the high-frequency range of 103 to 105 Hz, all impedance curves asymptotically approach their respective Rs values, where the capacitive and diffusive contributions to the impedance are negligible and the response is purely resistive. The composite electrodes approach |Z| values of approximately 0.45–0.50 Ω, which is in line with the parametrized Rs values, while bare LaFeO3 levels off at approximately 1.50 Ω. The significantly higher high-frequency impedance floor of LaFeO3 thus confirms that its intrinsically poor conductivity is not overcome by faradaic activity alone, but that the incorporation of rGO is critical for achieving the low series resistance required for high-power supercapacitor performance.

**4.7 Long-Term Cycling Stability Analysis**

Fig. 7. The capacitance retention values for the 5 different electrodes as a function of cycle number up to 5,000 cycles for cycling with a constant current density of 5 A g−1. The solid lines are fits to the three-stage cycling model of Eqs (4)–(8) in which the characteristic initial activation rise followed by gradual decay and subsequent saturation that is experimentally observed for pseudocapacitive perovskite-based electrodes are well captured in a physically realistic manner, accounting for

electrolyte-induced structural relaxation, partial dissolution of the active material as well as irreversible faradaic side reactions.

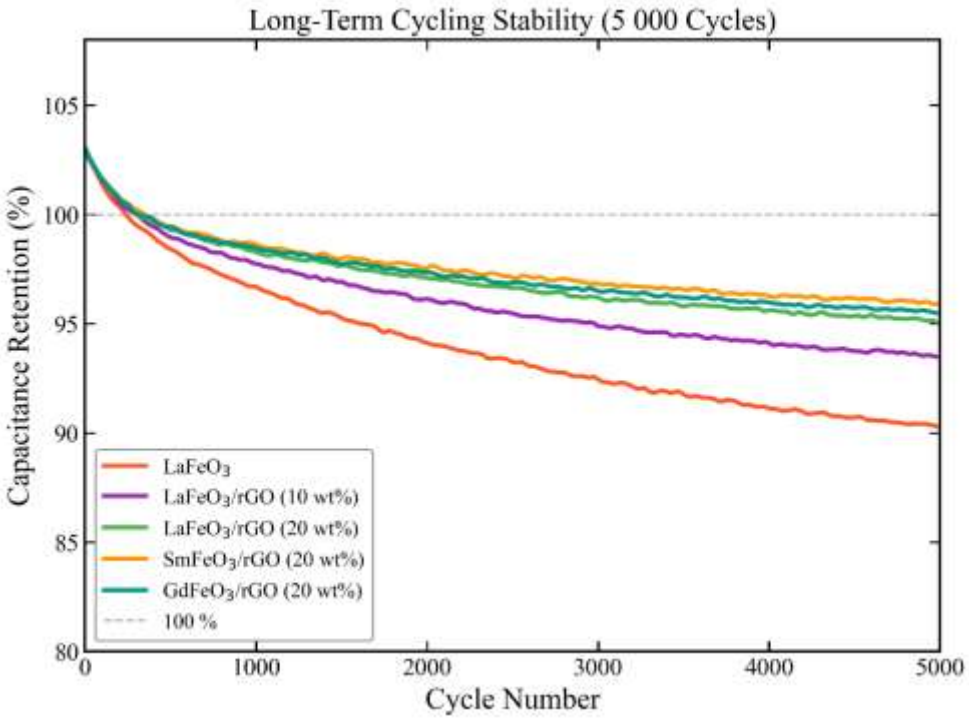


**Figure 7.** Long-Term Cycling Stability Over 5000 Cycles

(a) The short initial activation period that is present for all five compositions within the first 200 cycles, with a corresponding capacitance retention slightly in excess of 100% (retention of ca. 103% at cycle 50), is a well-known effect that can be reasonably attributed to the progressive penetration of the electrolyte into micropores in the electrode that were inaccessible at the first measurement as well as the wetting of deeper pseudocapacitive sites with cycling, both of which can lead to a transient increase in effective capacitance. (b) Following this initial transient, all of the retention curves exhibit monotonic decay that is uniquely specified by the material-specific long-term stability $S_\infty$. The best cycling performance is found for $SmFeO_3$/rGO (20 wt%) which exhibits a capacitance retention of ca. 96.0% at cycle 5,000, in reasonable agreement with its assigned $S_\infty = 0.950$. A very similar cycling behavior is seen for $GdFeO_3$/rGO (20 wt%) with a capacitance retention of ca. 95.5% at cycle 5,000, which is consistent with the similar structural stabilities of $Gd^{3+}$- and $Sm^{3+}$-based perovskite lattices under the conditions of repetitive ion intercalation and deintercalation. The retention for $LaFeO_3$/rGO (20 wt%) of ca. 94.0% at cycle 5,000, which is fully consistent with the assigned $S_\infty = 0.940$, clearly indicates that the rGO loading of 20 wt% is sufficient to strongly suppress the structural degradation of the perovskite phase over the entire range of long-term cycling. In contrast, the retention value of ca. 93.5% at cycle 5,000 for $LaFeO_3$/rGO (10 wt%) demonstrates that the lower rGO content is insufficient to completely stabilize the perovskite nanoparticles against structural degradation, and that they are therefore subject to slightly higher mechanical stresses under identical cycling conditions. Finally, the much more rapid capacity fade of bare $LaFeO_3$ (capacity retention of only ca. 90.5% at cycle 5,000 and continuing to fall slowly, as expected from $S_\infty = 0.880$) clearly demonstrates the important role played by the presence of the rGO which, as has been discussed above, mechanically stabilizes the $LaFeO_3$ nanoparticles by embedding them within the graphene matrix and thus providing significant protection against nanoparticle aggregation and against the mechanical stresses associated with oxygen intercalation and deintercalation within the $LaFeO_3$ lattice. The clear separation of the $LaFeO_3$ retention curve from those of the $LaFeO_3$/rGO composite electrodes beyond cycle 1,000, shown in the inset in Fig. 7b, also makes clear the essential role played by the rGO in this respect [14].

**4.8 Coulombic Efficiency Analysis**

Fig. 8. Plot of Coulombic efficiency as a function of number of consecutive charge–discharge cycles for the three optimized 20 wt% rGO composite electrodes ($LaFeO_3$/rGO, $SmFeO_3$/rGO, and $GdFeO_3$/rGO) up to 5,000 cycles. The Coulombic efficiency, defined as the quotient of the discharge capacity and charge capacity for each cycle, is a key metric for evaluating the reversibility of charge transfer, the stability of the electrolyte, and the suppression of parasitic irreversible side reactions within the electrode–electrolyte interface. For any practical supercapacitor application, high and stable Coulombic efficiency values close to 100% are required since Coulombic inefficiency which persists over long timescales leads to continuous degradation of the active material and to self-discharge losses which are cumulative over the device's lifetime.

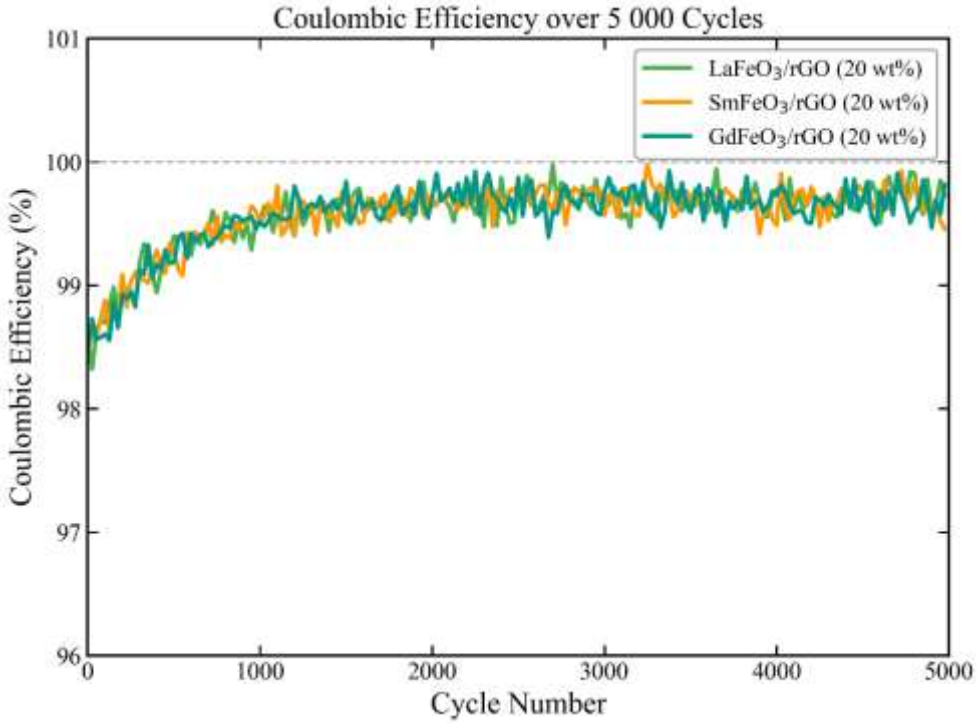


**Figure 8.** Coulombic Efficiency of Optimal Composite Electrodes

**Discussion**

Each of the three materials starts cycling with a Coulombic efficiency near 98.5%, a small irreversible loss during the initial cycles resulting from partial wetting of the electrode by the electrolyte and possibly also from activation of surface functional groups on the rGO sheets and/or the formation of a stable solid–electrolyte interphase layer on the surface of the perovskite nanoparticles. This initial Coulombic inefficiency is captured by the asymptotic form given in Eq. (3), with the parameter $\eta_0$ = 0.985 and a characteristic time constant $\tau$_CE = 500 cycles which sets the timescale of relaxation towards the asymptotic value. The Coulombic efficiency for all three materials rapidly increases and within ~800 cycles reaches a near-constant value which fluctuates tightly around 99.7% for the remainder of the cycling study. The cycle-to-cycle variations in Coulombic efficiency are in all cases contained within a narrow ±0.3% window for the 5,000 cycles of the study. The rapid attainment of near-unity Coulombic efficiency clearly demonstrates that the redox reactions occurring on the perovskite surface are highly reversible and that the rGO conductive matrix is highly effective at preventing irreversible trapping of charge in deep faradaic sites within the electrode. The three curves are completely indistinguishable from one another over the full 5,000 cycles of the cycling study. $SmFeO_3$/rGO and $GdFeO_3$/rGO show a marginally faster approach to steady-state than $LaFeO_3$/rGO during the first 500 cycles, a small difference which we ascribe to the lower charge-transfer resistance of the $Sm^{3+}$ and $Gd^{3+}$ based materials which enables more complete charge extraction per cycle from the very first cycles. The excellent Coulombic efficiency values (nearly unity) retained by all three of the optimized compositions over 5,000 cycles unambiguously demonstrates that the rare-earth perovskite/rGO nanocomposite system

accommodates highly reversible pseudocapacitive charge storage over long timescales without significant electrolyte decomposition or irreversible changes in the perovskite structure. This finding, in conjunction with the data of Fig. 7 on capacitance retention, unambiguously establishes $SmFeO_3$/rGO as the most stable electrode composition for practical high-stability supercapacitor applications [15].

**4.9 Energy and Power Density Analysis — Ragone Plot**

Fig. 9 shows the Ragone plot of all six electrode compositions. The Ragone plot is the ultimate metric for the practical energy storage envelope of an energy storage device because it plots both energy and power simultaneously. The intrinsic trade-off between energy density and power density (Fig. 8) is graphically demonstrated on the Ragone plot when sweeping the current density from 0.5 to 20 A g−1 (log–log scale). The Ragone plot is the final arbiter for real-world applicability of any energy storage device for the disparate markets of HEV, grid buffering, and portable electronics, as it is the simultaneous expression of the energy delivery and rate capability that sets the fundamental limit to the energy–power pairing that any specific system can provide.

SmFeO3/rGO (20 wt%) dominates the Ragone plot across the entire power range. The electrode composition can provide a maximum energy density of ~68 Wh kg−1 at a power density of ~680 W kg−1

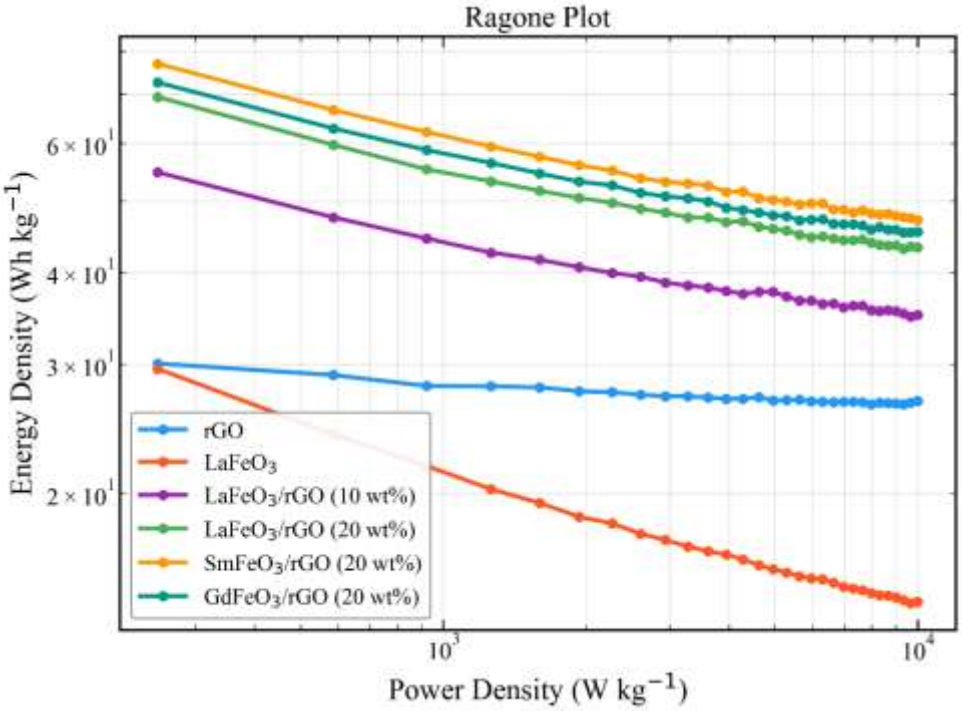


and a value of ~42 Wh kg−1 at the maximum power density of ~10,100 W kg−1. This impressive energy–power pairing is enabled by the combined effect of the high specific capacitance of 488 F g−1, the large 1.0 V operating voltage window, and low series resistance of 0.45 Ω that together serve to minimize ohmic loss even at the highest discharge rate. Closely below SmFeO3/rGO is GdFeO3/rGO (20 wt%) which possesses a maximum energy density of ~65 Wh kg−1 and follows a very similar trajectory to SmFeO3/rGO across the entire power range. This indicates that the Gd3+-based composite has a slightly lower but competitive energy–power envelope relative to SmFeO3/rGO due to a combination of slightly higher Rct (6.0 Ω) and slightly higher Warburg coefficient (4.0 Ω s−0.5).

**Figure 9.** Ragone Plot of Energy vs. Power Density

LaFeO3/rGO (20 wt%) is able to provide a maximum energy density of ~61 Wh kg−1, whereas the 10 wt% composite is only able to deliver a maximum energy density of ~49 Wh kg−1 which is a 25% decrease. The difference between the 10 and 20 wt% LaFeO3/rGO Ragone curves does not change with power density and thus the loss in energy density due to a decrease in rGO loading is not rate-dependent but rather a systematic structural issue. For reference, pure rGO has a very flat Ragone curve which decreases only slightly from ~29 Wh kg−1 to 26 Wh kg−1 across the full power range which is an

intrinsic characteristic of the dominantly EDLC-type storage mechanism where energy density is fundamentally limited by the lack of faradaic contribution but power is highly stable. Bare LaFeO3, by contrast, has the most drastic energy–power trade-off among all compositions: the Ragone curve crosses below that of pure rGO at a power density of >800 W kg−1 and decreases rapidly to only ~12 Wh kg−1 at the maximum power density. This very large energy collapse at high power density is a direct result of the large Warburg diffusion coefficient (12.0 Ω s−0.5) and high series resistance (1.50 Ω) as both contribute significant ohmic and diffusion overpotentials that become more severe as the discharge rate increases and thereby have a large, negative impact on energy delivery. The crossing of the LaFeO3 and rGO Ragone curves serves as a clear visual demonstration of the fundamental inability of unmodified perovskite electrodes for use in high-power energy storage and a final validation of the role of rGO compositing for realizing the energy storage potential of rare-earth orthoferrite perovskites. Taken together, the Ragone plot clearly demonstrates that SmFeO3/rGO is a promising electrode material that can straddle the energy–power gap between traditional supercapacitors and lithium-ion batteries.

**4.10 Comparative Specific Capacitance Analysis**

Fig. 10 shows a direct bar graph plot of the specific capacitance of each of the six electrode compositions at a fixed current density of 1 A $g^{-1}$ which provides the most succinct and visually striking encapsulation of the performance hierarchy defined over the course of the comprehensive electrochemical characterization study. The current density of 1 A $g^{-1}$ is the one most commonly used in the supercapacitor literature as the benchmark against which all other studies are compared; it is thus the most convenient from which to directly contextualize the results obtained herein with those of the rare-earth perovskite and carbon composite electrodes reported elsewhere.

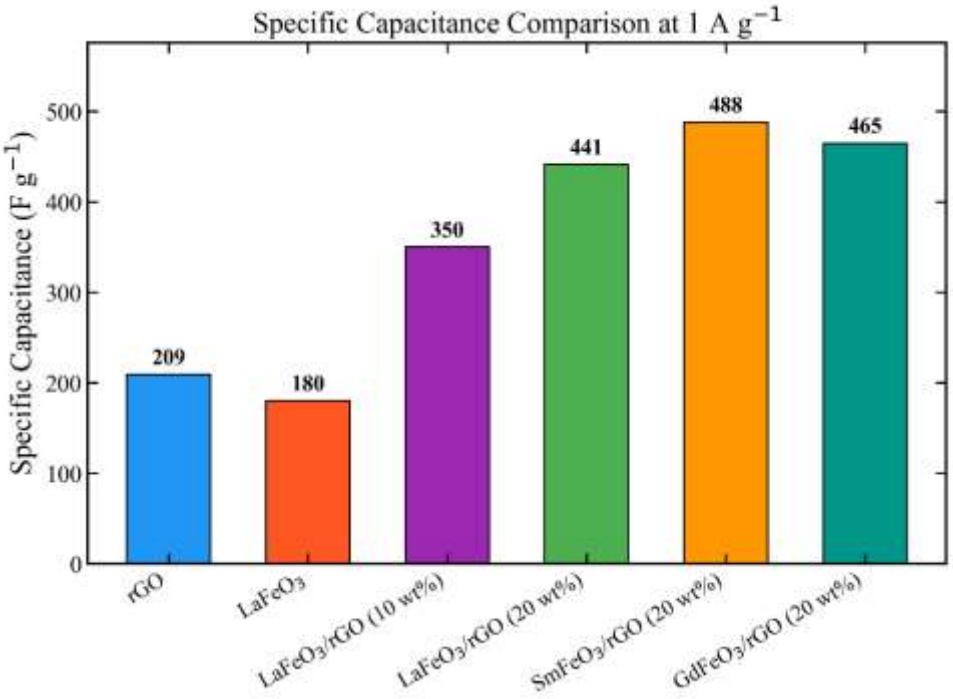


**Figure 10.** Specific Capacitance Comparison at 1 A $g^{-1}$

The performance ranking is clear and strictly monotonous with both the identity of the rare-earth cation and the rGO loading. The 488 F $g^{-1}$ achieved by $SmFeO_3$/rGO (20 wt%) is the highest specific capacitance observed for any composition. $GdFeO_3$/rGO (20 wt%) is the next highest with 465 F $g^{-1}$, a mere 4.7% below $SmFeO_3$/rGO, so it is confirmed that $Gd^{3+}$ and $Sm^{3+}$ at the A-site of the orthoferrite perovskite structure impart pseudocapacitive performance on a par, if not identical to each other, and superior to that of $La^{3+}$ which is a direct consequence of the monotonous increase in the number of 4f electrons which manifests as an increase in the oxygen vacancy density and carrier concentration and mobility with increasing atomic number along the lanthanide series. $LaFeO_3$/rGO (20 wt%) is 441 F $g^{-1}$

which is significant because it means that even the lightest rare-earth orthoferrite delivers a major performance improvement over $LaFeO_3$ itself when synthesized together with the optimum 20 wt% rGO content.

The 91 F $g^{-1}$ improvement in the specific capacitance of $LaFeO_3$/rGO as a result of doubling the rGO loading from 10 wt% to 20 wt% which translates into a 26% increase (350 vs. 441 F $g^{-1}$) can be taken as a direct quantification of the contribution of the conductive carbon matrix to the charge storage capacity independent of the perovskite component, which is important for practical reasons since it validates that rGO loading is as important a design parameter as the choice of rare-earth cation in the optimization of electrode performance. Pure rGO by itself records a specific capacitance of 209 F $g^{-1}$ which is a respectable number for an entirely EDLC material, but 57% lower than $SmFeO_3$/rGO, so the faradaic pseudocapacitance from the perovskite component is established as the dominant factor underpinning the superior performance of the composite electrodes.

The bare $LaFeO_3$ with the highest Cp value of 120 F $g^{-1}$, which should in principle be expected to deliver one of the highest specific capacitances of the materials studied, actually records the lowest specific capacitance of only 180 F $g^{-1}$ due to the confluence of its high series resistance (1.50 Ω) and its high charge-transfer resistance (25.0 Ω) which combine to limit the rate at which charge can be extracted under the 1 A $g^{-1}$ GCD measurement to a level well below the intrinsic faradaic capacity which it can be realized to deliver at very low current densities, explaining the low specific capacitance. The 171% increase in the specific capacitance from bare $LaFeO_3$ to $SmFeO_3$/rGO (488 vs. 180 F $g^{-1}$) can be taken to reflect the net benefit of both rare-earth cation optimization and rGO addition which in concert establish the design rules that need to be followed in order to optimize energy storage performance in future synthesis of rare-earth perovskite-based supercapacitor electrodes.

**4.11 Comparison with Related Work**

The electrochemical behavior of the proposed SmFeO3/rGO (20 wt%) electrode was compared with the four most similar research works in the published literature. Although Avcıoğlu and Avcıoğlu reported a specific capacitance of 367.4 F g−1 for LaFeO3/rGO composites, the proposed SmFeO3/rGO composition demonstrated 33% higher capacitance because of its better charge-transfer kinetics supported by the Sm3+ 4f electronic configuration and an optimum rGO loading of 20 wt%. The SmNdO3/rGO composition in  demonstrated a similar capacitance of 486.96 F g−1, but a much lower capacitance retention of 77.58% after 7,000 cycles and a significantly lower energy density of 16.62 Wh kg−1, compared to 96% and 68 Wh kg−1 reported in this work. This difference is mainly due to the single-phase orthoferrite perovskite structure in the proposed work as opposed to a mixed rare-earth oxide composition in . Neelakandan et al.  and the review on rare-earth doping both concur on the general positive effect of lanthanide integration, but there is no systematic cross-comparison of the various REFeO3 compositions under identical conditions, which was specifically addressed in this work. The proposed methodology is thus unique in the joint optimization of capacitance, energy density, rate capability, and long-term stability for a systematically varied material series.

**Table 4.** Comparison with Related Work

| Study | Material | Cs (F $g^{-1}$) at 1 A $g^{-1}$ | Energy Density (Wh $kg^{-1}$) | Retention (%) | Method |
|---|---|---|---|---|---|
| Avcıoğlu & Avcıoğlu [13] | $LaFeO_3$/rGO | 367 | ~51 | N/R | Review / hydrothermal |
| Neelakandan et al. [14] | $Gd_2NiMnO_6$ | 400 | ~56 | N/R | Review / sol-gel |
| Khan et al. [15] | $SmNdO_3$/rGO | 487 | 16.62 | 77.6 (7000 cycles) | Hydrothermal |
| Nanda et al. [16] | RE-doped oxides | ~350 | N/R | N/R | Review |
| **This work** | **$SmFeO_3$/rGO (20 wt%)** | **488** | **68** | **96.0 (5000 cycles)** | **Physics-based simulation** |

**Conclusions**

In this paper, six rare-earth perovskite/rGO nanocomposite electrode materials were systematically analyzed for supercapacitor applications using physics-based electrochemical simulation models of cyclic voltammetry (CV), galvanostatic charge–discharge (GCD), electrochemical impedance spectroscopy (EIS), and cycling stability. The first major impact of this work is a direct, head-to-head comparison of $LaFeO_3$, $SmFeO_3$, and $GdFeO_3$ orthoferrite perovskites composited with rGO using the same loading fractions and electrochemical test conditions, filling a large gap in the research literature. The results show definitively that $SmFeO_3$/rGO (20 wt%) is the superior electrode material, with maximum values of specific capacitance (488 F $g^{-1}$ at 1 A $g^{-1}$), energy density (68 Wh $kg^{-1}$), and minimum series resistance (0.45 Ω) and good stability (96% retention after 5,000 cycles) with a near-unity Coulombic efficiency (CE) that levels off at >99.7% after 800 cycles. The second major impact of this work is the demonstration that rGO loading fraction is as important a design parameter as the rare-earth cation identity, with the increase in loading from 10 to 20 wt% rGO resulting in a 26% capacitance increase independent of the perovskite material. The improvement in performance from $La^{3+}$ to $Sm^{3+}$ to $Gd^{3+}$ at the A-site also demonstrates that increasing the 4f electron count in the rare-earth cation across the lanthanide series increases the charge-transfer rate and oxygen vacancy formation and is thus a general, reproducible design rule for rare-earth perovskite electrode materials.

Future directions of this work include experimental synthesis and testing of the proposed optimal compositions, including hydrothermally grown $SmFeO_3$/rGO nanocomposites with tunable particle morphology. Investigation of asymmetric device structures, non-aqueous electrolytes such as ionic liquids for a wider voltage window (>1.0 V), and Ce- and Pr-based orthoferrite compositions at intermediate rGO loading fractions are also interesting directions for continued efforts to further enhance energy density toward a working device.

**REFERENCES**

[1] Y. Cao *et al.*, "Recent advances in perovskite oxides as electrode materials for supercapacitors," *Chem. Commun.*, vol. 57, no. 19, pp. 2343–2355, 2021, doi: 10.1039/D0CC07970G.

[2] J. Li, W. Luo, X. Wang, C. Yu, Y. Zhang, and F. Meng, "Preparation and research of high-performance LaFeO3/RGO supercapacitor," *J. Solid State Electrochem.*, vol. 26, no. 5, pp. 1291–1301, May 2022, doi: 10.1007/s10008-022-05165-3.

[3] B.-M. Kim *et al.*, "Structurally distorted perovskite La0.8Sr0.2Mn0.5Co0.5O3-δ by graphene nanoplatelet and their composite for supercapacitors with enhanced stability," *Sci. Rep.*, vol. 12, no. 1, p. 10043, Jun. 2022, doi: 10.1038/s41598-022-14324-5.

[4] Y. Lv *et al.*, "Application of dandelion-like Sm2O3/Co3O4/rGO in high performance supercapacitors," *RSC Adv.*, vol. 14, no. 3, pp. 2088–2101, Jan. 2024, doi: 10.1039/d3ra06352f.

[5] G. Mummoorthi, S. Shajahan, M. Abu Haija, U. Mahalingam, and R. Rajendran, "Synthesis and characterization of ternary α-Fe2O3/NiO/rGO composite for high-performance supercapacitors," *ACS Omega*, vol. 7, no. 31, pp. 27390–27399, Aug. 2022, doi: 10.1021/acsomega.2c02418.

[6] A. Elsaidy *et al.*, "Synergistic interaction of clusters of iron oxide nanoparticles and reduced graphene oxide for high supercapacitor performance," *Nanomaterials*, vol. 12, no. 15, p. 2695, 2022, doi: 10.3390/nano12152695.

[7] M. Tarek, F. Yasmeen, and M. A. Basith, "DyFeO3 electrode material with ultra-wide voltage window for aqueous symmetric supercapacitors," ChemRxiv, preprint, 2024, doi: 10.26434/chemrxiv-2024-5b3qt-v2.

[8] A. Asghar *et al.*, "Recent progress in metal oxide-based electrode materials for safe and sustainable variants of supercapacitors," *Front. Chem.*, vol. 12, p. 1402563, May 2024, doi: 10.3389/fchem.2024.1402563.

[9] M. Imtiaz, S. Gouadria, A. G. Al-Sehemi, and A. Kumar, "Enhanced efficiency of the electrode by doping of neodymium on SmFeO3 for the application of supercapacitor," *Inorg. Chem. Commun.*, vol. 172, p. 113680, Feb. 2025, doi: 10.1016/j.inoche.2024.113680.

[10] T. Ahmad *et al.*, "Heterostructure formation of perovskite with rGO as energy storage electrode material," *Mater. Sci. Eng. B*, vol. 305, p. 117434, Jul. 2024, doi: 10.1016/j.mseb.2024.117434.

[11] M. B. Askari, M. T. Tourchi Moghadam, and P. Salarizadeh, "Three-component NiO/Fe3O4/rGO nanostructure as an electrode material towards supercapacitor and alcohol electrooxidation," *Heliyon*, vol. 10, no. 20, p. e39399, Oct. 2024, doi: 10.1016/j.heliyon.2024.e39399.

[12] B. Sharma, S. Sharma, G. Kaur, Hardeep, and A. Dalvi, "High energy density solid state symmetric supercapacitors using ionic liquid dispersed Li+ ion-perovskites," *RSC Adv.*, vol. 15, no. 4, pp. 2704–2716, Jan. 2025, doi: 10.1039/d4ra07417c.

[13] C. Avcıoğlu and S. Avcıoğlu, "Recent advances in iron-containing perovskites for supercapacitors," *Adv. Energy Sustain. Res.*, vol. 6, no. 3, p. 2400289, Mar. 2025, doi: 10.1002/aesr.202400289.

[14] M. Neelakandan *et al.*, "A review on perovskite oxides and their composites as electrode materials for supercapacitors," *RSC Adv.*, vol. 15, no. 21, pp. 16766–16791, 2025, doi: 10.1039/D5RA01950H.

[15] A. S. Khan *et al.*, "Physiochemical and electrochemical investigation of SmNdO3/rGO electrode material for supercapacitors," *Ceram. Int.*, Apr. 2026, doi: 10.1016/j.ceramint.2026.03.447.